



Pelphix: Surgical Phase Recognition from X-Ray Images in Percutaneous Pelvic Fixation

Benjamin D. Killeen^(✉), Han Zhang, Jan Mangulabnan,
Mehran Armand, Russell H. Taylor, Greg Osgood,
and Mathias Unberath

Johns Hopkins University, Baltimore, MD, USA
{killeen,hzhan206,jmangul1,rht,unberath}@jhu.edu,
{marmand2,gosgood2}@jhmi.edu

Abstract. Surgical phase recognition (SPR) is a crucial element in the digital transformation of the modern operating theater. While SPR based on video sources is well-established, incorporation of interventional X-ray sequences has not yet been explored. This paper presents Pelphix, a first approach to SPR for X-ray-guided percutaneous pelvic fracture fixation, which models the procedure at four levels of granularity – corridor, activity, view, and frame value – simulating the pelvic fracture fixation workflow as a Markov process to provide fully annotated training data. Using added supervision from detection of bony corridors, tools, and anatomy, we learn image representations that are fed into a transformer model to regress surgical phases at the four granularity levels. Our approach demonstrates the feasibility of X-ray-based SPR, achieving an average accuracy of 99.2% on simulated sequences and 71.7% in cadaver across all granularity levels, with up to 84% accuracy for the target corridor in real data. This work constitutes the first step toward SPR for the X-ray domain, establishing an approach to categorizing phases in X-ray-guided surgery, simulating realistic image sequences to enable machine learning model development, and demonstrating that this approach is feasible for the analysis of real procedures. As X-ray-based SPR continues to mature, it will benefit procedures in orthopedic surgery, angiography, and interventional radiology by equipping intelligent surgical systems with situational awareness in the operating room. Code and data available at <https://github.com/benjamindkilleen/pelphix>.

Keywords: Activity recognition · fluoroscopy · orthopedic surgery · surgical data science

Supplementary Information The online version contains supplementary material available at https://doi.org/10.1007/978-3-031-43996-4_13.

© The Author(s), under exclusive license to Springer Nature Switzerland AG 2023
H. Greenspan et al. (Eds.): MICCAI 2023, LNCS 14228, pp. 133–143, 2023.
https://doi.org/10.1007/978-3-031-43996-4_13

1 Introduction

In some ways, surgical data is like the expanding universe: 95% of it is dark and unobservable [2]. The vast majority of intra-operative X-ray images, for example, are “dark”, in that they are not further analyzed to gain quantitative insights into routine practice, simply because the human-hours required would drastically outweigh the benefits. As a consequence, much of this data not only goes un-analyzed but is discarded directly from the imaging modality after inspection. Fortunately, machine learning algorithms for automated intra-operative image analysis are emerging as an opportunity to leverage these data streams. A popular application is surgical phase recognition (SPR), a way to obtain quantitative analysis of surgical workflows and equip automated systems with situational awareness in the operating room (OR). SPR can inform estimates of surgery duration to maximize OR throughput [7] and augment intelligent surgical systems, *e.g.* for suturing [20] or image acquisition [4, 10, 11], enabling smooth transitions from one specialized subsystem to the next. Finally, SPR provides the backbone for automated skill analysis to produce immediate, granular feedback based on a specific surgeon’s performance [5, 21].

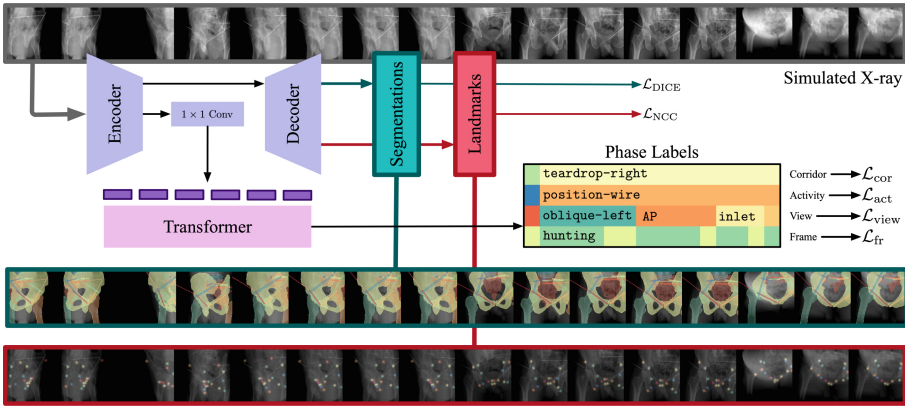


Fig. 1. Our model architecture incorporates frame-level spatial annotations using a U-Net encoder-decoder variant. Anatomical landmarks and segmentation maps provide added supervision to the image encoder for a transformer, which predicts the surgical phase. The images shown here are the result of Markov-based simulation of percutaneous fixation, used for training.

The possibilities described above have motivated the development of algorithms for surgical phase recognition based on the various video sources in the OR [15, 19, 22, 23]. However, surgical phase recognition based on interventional X-ray sequences remains largely unexplored. Although X-ray guidance informs more than 17 million procedures across the United States (as of 2006) [13], the unique challenges of processing X-ray sequences compared to visible or structured light

imaging have so far hindered research in this area. Video cameras collect many images per second from relatively stationary viewpoints. By contrast, C-arm X-ray imaging often features consecutive images from vastly different viewpoints, resulting in highly varied object appearance due to the transmissive nature of X-rays. X-ray images are also acquired irregularly, usually amounting to several hundred frames in a procedure of several hours, limiting the availability of training data for machine learning algorithms.

Following recent work that enables sim-to-real transfer in the X-ray domain [6], we now have the capability to train generalizable deep neural networks (DNNs) using simulated images, where rich annotations are freely available. *This paper represents the first step in breaking open SPR for the X-ray domain, establishing an approach to categorizing phases, simulating realistic image sequences, and analyzing real procedures.* We focus our efforts on percutaneous pelvic fracture fixation, which involves the acquisition of standard views and the alignment of Kirschner wires (K-wires) and orthopedic screws with bony corridors [17]. We model the procedure at four levels, the current target corridor, activity (**position-wire**, **insert-wire**, and **insert-screw**), C-arm view (**AP**, **lateral**, etc.), and frame-level clinical value. Because of radiation exposure for both patients and clinicians, it is relevant to determine which X-ray images are acquired in the process of “fluoro-hunting” (**hunting**) versus those used for clinical **assessment**. Each of these levels is modeled as a Markov process in a stochastic simulation, which provides fully annotated training data for a transformer architecture.

2 Related Work

SPR from video sources is a popular topic, and has benefited from the advent of transformer architectures for analyzing image sequences. The use of convolutional layers as an image encoder has proven effective for recognizing surgical phases in endoscopic video [22] and laparoscopic video [3, 19]. These works especially demonstrate the effectiveness of transformers for dealing with long image sequences [3], while added spatial annotations improve both the precision and information provided by phase recognition [19]. Although some work explores activity recognition in orthopedic procedures [8, 9] they rely on head-mounted cameras with no way to assess tool-to-tissue relationships in percutaneous procedures. The inclusion of X-ray image data in this space recenters phase recognition on patient-centric data and makes possible the recognition of surgical phases which are otherwise invisible.

3 Method

The Pelphix pipeline consists of stochastic simulation of X-ray image sequences, based on a large database of annotated CT images, and a transformer architecture for phase recognition with additional task-aware supervision. A statistical shape model is used to propagate landmark and corridor annotations over 337

CTs, as shown in Fig. 2a. The simulation proceeds by randomly aligning virtual K-wires and screws with the annotated corridors (Sect. 3.1). In Sect. 3.2, we describe a transformer architecture with a U-Net style encoder-decoder structure enables sim-to-real transfer for SPR in X-ray.

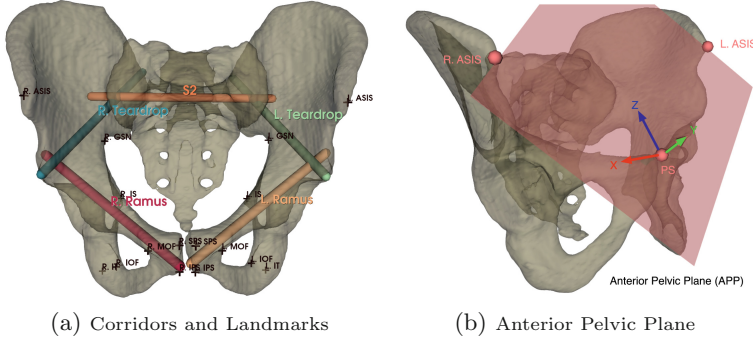


Fig. 2. (a) The ramus, teardrop and S2 bony corridors, as well as 16 anatomical landmarks with added supervision for phase recognition. (b) The anterior pelvic plane (APP) coordinate system is used to define principle ray directions for standard views of the pelvis, enabling realistic simulation of image sequences for percutaneous fixation.

3.1 Image Sequence Simulation for Percutaneous Fixation

Unlike sequences collected from real surgery [15] or human-driven simulation [14], our workflow simulator must capture the procedural workflow while also maintaining enough variation to allow algorithms to generalize. We accomplish this by modeling the procedural state as a Markov process, in which the transitions depend on evaluations of the projected state, as well as an adjustment factor $\lambda_{\text{adj}} \in [0, 1]$ that affects the number of images required for a given task. A low adjustment factor decreases the probability of excess acquisitions for the simulated procedure. In our experiments, we sample $\lambda_{\text{adj}} \in \mathcal{U}(0.6, 0.8)$ at the beginning of each sequence.

Figure 3 provides an overview of this process. Given a CT image with annotated corridors, we first sample a target corridor with start and endpoints $\mathbf{a}, \mathbf{b} \in \mathbb{R}^3$. For the ramus corridors, we randomly swap the start and endpoints to simulate the retrograde and antegrade approaches. We then uniformly sample the initial wire tip position within 5 mm of \mathbf{a} and the direction within 15° of $\mathbf{b} - \mathbf{a}$.

Sample Desired View. The desired view is sampled from views appropriate for the current target corridor. For example, appropriate views for evaluating wire placement in the superior ramus corridor are typically the inlet and obturator oblique views, and other views are sampled with a smaller probability. We refer to the “oblique left” and “oblique right” view independent of the

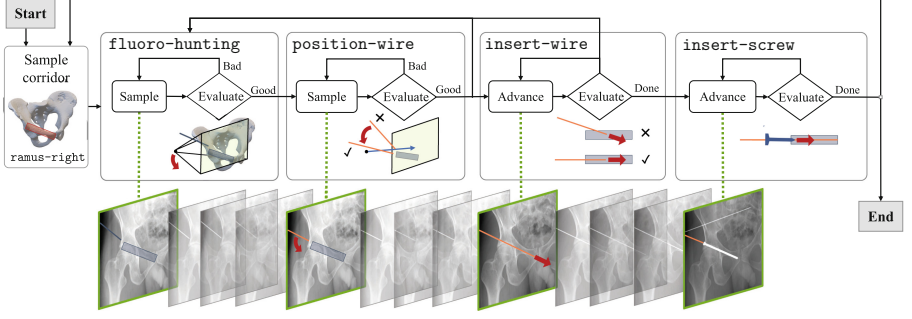


Fig. 3. The image sequence simulation pipeline for Pelphix. We model the procedure as a Markov random process, where transition probabilities depend on realistic evaluation of the current frame.

affected patient side, so that for the right pubic ramus, the obturator oblique is the “oblique left” view, and the iliac oblique is “oblique right.” We define the “ideal” principle ray direction $\hat{\mathbf{r}}^*$ for each standard view in the anterior pelvic plane (APP) coordinate system (see supplement) and the ideal viewing point \mathbf{p}^* as the midpoint of the target corridor. At the beginning of each sequence, we sample the intrinsic camera matrix of the virtual C-arm with sensor width $w_s \sim \mathcal{U}(300, 400)$ mm, $d_{sd} \sim \mathcal{U}(900, 1200)$, and an image size of 384×384 . Given a viewing point and direction $(\mathbf{p}, \hat{\mathbf{r}})$, the camera projection matrix \mathbf{P} is computed with the X-ray source (or camera center) at $\mathbf{p} - d_{sp}\hat{\mathbf{r}}$ and principle ray $\hat{\mathbf{r}}$, where $d_{sp} \sim \mathcal{U}(0.65 d_{sd}, 0.75 d_{sd})$ is the source-to-viewpoint distance, and d_{sd} is the source-to-detector distance (or focal length) of the virtual C-arm.

Evaluate View. Given a current view $(\mathbf{p}, \hat{\mathbf{r}})$ and desired view $(\mathbf{p}^*, \hat{\mathbf{r}}^*)$, we first evaluate whether the current view is acceptable and, if it is not, make a random adjustment. View evaluation considers the principle ray alignment and whether the viewing point is reasonably centered in the image, computing,

$$\hat{\mathbf{r}} \cdot \hat{\mathbf{r}}^* < \cos(\theta_t) \text{ AND } \left\| \mathbf{P}\mathbf{p}^* - \begin{bmatrix} \frac{H}{2} & \frac{W}{2} & 1 \end{bmatrix}^T \right\| < \frac{2}{5} \min(H, W) \quad (1)$$

where the angular tolerance $\theta_t \in [3^\circ, 10^\circ]$ depends on the desired view, ranging from teardrop views (low) to lateral (high tolerance).

Sample View. If Eq. 1 is not satisfied, then we sample a new view $(\mathbf{p}, \hat{\mathbf{r}})$ uniformly within a uniform window that shrinks every iteration by the adjustment factor, according to

$$\mathbf{p} \sim \mathcal{U}_o(\mathbf{p}^*, \text{clip}(\lambda_{\text{adj}} \|\mathbf{p}^* - \mathbf{p}\|, 5 \text{ mm}, 100 \text{ mm})) \quad (2)$$

$$\hat{\mathbf{r}} \sim \mathcal{U}_\angle(\hat{\mathbf{r}}^*, \text{clip}(\lambda_{\text{adj}} \arccos(\hat{\mathbf{r}}^* \cdot \hat{\mathbf{r}}), 1^\circ, 45^\circ)), \quad (3)$$

where $\mathcal{U}_o(\mathbf{c}, r)$ is the uniform distribution in the sphere with center \mathbf{c} and radius r , and $\mathcal{U}_\angle(\hat{\mathbf{r}}, \theta)$ is the uniform distribution on the solid angle centered on $\hat{\mathbf{r}}$ with

colatitude angle θ . This formula emulates observed fluoro-hunting by converging on the desired view until a point, when further adjustments are within the same random window [12]. We proceed by alternating view evaluation and sampling until evaluation is satisfied, at which point the simulation resumes with the current activity: wire positioning, wire insertion, or screw insertion.

Evaluate Wire Placement. During wire positioning, we evaluate the current wire position and make adjustments from the current view, iterating until evaluation succeeds. Given the current wire tip \mathbf{x} , direction $\hat{\mathbf{v}}$, and projection matrix \mathbf{P} , the wire placement is considered “aligned” if it *appears* to be aligned with the projected target corridor in the image, modeled as a cylinder. In addition, we include a small likelihood of a false positive evaluation, which diminishes as the wire is inserted.

Sample Wire Placement. If the wire evaluation determines the current placement is unsuitable, then a new wire placement is sampled. For the down-the-barrel views, this is done similarly to Eq. 2, by bringing the wire closer to the corridor in 3D. For orthogonal views, repositioning consists of a small random adjustment to \mathbf{x} , a rotation about the principle ray (the in-plane component), and a minor perturbation orthogonal to the ray (out-of-plane). This strategy emulates real repositioning by only adjusting the degree of freedom visible in the image, i.e. the projection onto the image plane:

$$\mathbf{x} \sim \mathcal{U}_o(\mathbf{x}, \text{clip}(\lambda_{\text{adj}} \|\mathbf{x} - \mathbf{a}\|, 5 \text{ mm}, 10 \text{ mm})) \quad (4)$$

$$\hat{\mathbf{v}} \leftarrow \text{Rot}(\hat{\mathbf{v}} \times \hat{\mathbf{r}}, \theta_{\perp}) \text{Rot}(\hat{\mathbf{r}}, \theta^* + \theta_{\parallel}), \text{ where } \theta_{\perp} \sim \mathcal{U}(-0.1\theta^*, 0.1\theta^*), \quad (5)$$

$$\theta_{\parallel} \sim \mathcal{U}(-\text{clip}(\lambda_{\text{adj}}\theta^*, 3^\circ, 10^\circ), \text{clip}(\lambda_{\text{adj}}\theta^*, 3^\circ, 10^\circ)), \quad (6)$$

and θ^* is the angle between the wire and the target corridor in the image plane. If the algorithm returns “Good,” the sequence either selects a new view to acquire (and stays in the **position-wire** activity) or proceeds to **insert-wire** or **insert-screw**, according to random transitions.

In our experiments, we used 337 CT images: 10 for validation, and 327 for generating the training set. (Training images were collected continuously during development, after setting aside a validation set.) A DRR was acquired at every decision point in the simulation, with a maximum of 1000 images per sequence, and stored along with segmentations and anatomical landmarks. We modeled a K-wire with 2 mm diameter and orthopedic screws with lengths from 30 to 130 mm and a 16 mm thread, with up to eight instances of each in a given sequence. Using a customized version of DeepDRR [18], we parallelized image generation across 4 RTX 3090 GPUs with an observed GPU memory footprint of ~ 13 GB per worker, including segmentation projections. Over approximately five days, this resulted in a training set of 677 sequences totaling 279,709 images and 22 validation sequences with 8,515 images.

3.2 Transformer Architecture for X-ray-based SPR

Figure 1 shows the transformer architecture used to predict surgical phases based on embedding tokens for each frame. To encourage local temporal features in each

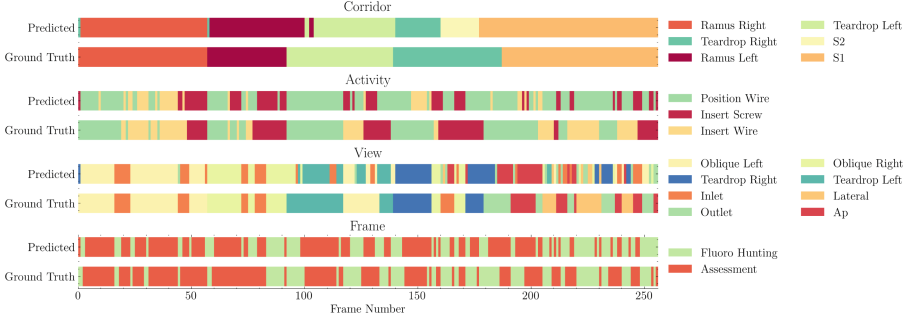


Fig. 4. Results of surgical phase recognition for a cadaveric procedure. We observe varying performance based on the target corridor, either because of the associated views or due to the accumulated orthopedic hardware.

embedding token, we cross-pollinate adjacent frames in the channel dimension, so that each $(3, H, W)$ encoder input contains the previous, current, and next frame. The image encoder is a U-Net [16] encoder-decoder variant with 5 Down and Up blocks and 33 spatial output channels, consisting of (a) 7 segmentation masks of the left hip, right hip, left femur, right femur, sacrum, L5 vertebra, and pelvis; (b) 8 segmentation masks of bony corridors, including the ramus (2), teardrop (2) and sacrum corridors (4), as in Fig. 2a; (c) 2 segmentation masks for wires and screws; and (d) 16 heatmaps corresponding to the anatomical landmarks in Fig. 2a. These spatial annotations provide additional supervision, trained with DICE loss $\mathcal{L}_{\text{DICE}}$ for segmentation channels and normalized cross correlation \mathcal{L}_{NCC} for heatmap channels as in [1, 6]. To compute tokens for input to the transformer, we apply a 1×1 Conv + BatchNorm + ReLU block with kernel size 512 to the encoder output, followed by global average pooling. The transformer has 6 layers with 8 attention heads and a feedforward dimension of 2048. During training and inference, we apply forward masking so that only previous frames are considered. The output of the transformer are vectors in \mathbb{R}^{21} with phase predictions for each frame, corresponding to (a) the 8 target corridors; (b) 3 activities (**position-wire**, **insert-wire**, or **insert-screw**); (c) 8 standard views (see Sect. 3.1); and (d) 2 frame values (**hunting** or **assessment**). We compute the cross entropy loss separately for the corridor \mathcal{L}_{cor} , activity \mathcal{L}_{act} , view $\mathcal{L}_{\text{view}}$, and frame \mathcal{L}_{fr} phases, and take the mean.

Training Details. Following [6, 11], we use a pipeline of heavy domain randomization techniques to enable sim-to-real transfer. In our experiments, we trained the transformer for 200 epochs on 2 RTX 3090 GPUs with 24 GB of memory each, with a sequence length of 48 and a batch size of 4. The initial learning rate was 0.0001, reduced by a factor of 10 at epoch 150 and 180.

4 Evaluation

Simulation. We report the results of our approach first on simulated image sequences, generated from the withheld set of CT images, which serves as an upper bound on real X-ray performance. In this context our approach achieves an accuracy of 99.7%, 98.2%, 99.8%, and 99.0% with respect to the corridor, activity, view, and frame level, respectively. Moreover, we achieve an average DICE score of 0.72 and landmark detection error of 1.01 ± 0.153 pixels in simulation, indicating that these features provide a meaningful signal. That the model generalizes so well to the validation set reflects the fact that these sequences are sampled using the same Markov-based simulation as the training data.

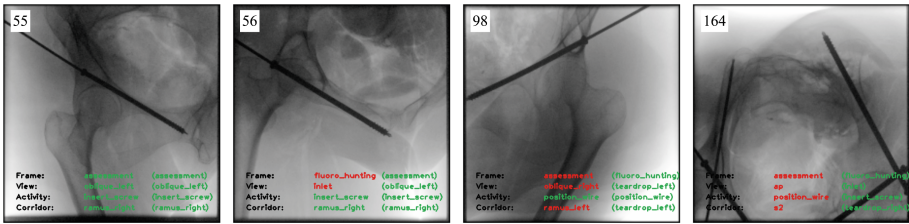


Fig. 5. Exemplary cases from the cadaver study. Image 55 is an ideal prediction, whereas image 56 merely confirms the final placement. Image 98 illustrates an ambiguity that can arise between the teardrop and oblique views during fluoro-hunting, while image 164 is interpreted as belonging to an S2 insertion.

Cadaver Study. We evaluate our approach on cadaveric image sequences with five screw insertions. An attending orthopedic surgeon performed percutaneous fixation on a lower torso specimen, taking the antegrade approach for the left and right pubic ramus corridors, followed by the left and right teardrop and S1 screws. An investigator acted as the radiological technician, positioning a mobile C-arm according to the surgeon’s direction. A total of 257 images were acquired during these fixations, with phase labels based on the surgeon’s narration.

Our results, shown in Fig. 4 demonstrate the potential for Pelpix as a viable approach to SPR in X-ray. We achieve an overall accuracy of 84%, 60%, 65%, and 77% with respect to the corridor, activity, view, and frame levels, respectively. Figure 5 shows exemplary success and failure modes for our approach, which struggles with ambiguities that may arise due to the similarity of certain views. For instance, image 98 was acquired during fluoro-hunting for the teardrop left view, but our approach associates this sequence with verification of the left ramus screw, which was just finished. Similarly, after the right teardrop wire was inserted, our approach anticipated the insertion of an S2 wire. This was a valid transition in our simulation, so surgeon preferences may be needed to resolve the ambiguity. At the same time, we observe significantly higher accuracy for the pubic ramus corridors (97.7, 76.9, 98.3, and 84.4% respectively) than the teardrop (60.2, 56.9, 64.2, 73.7%) and S1 corridors (100%, 40.6%, 23%, 71%), which may reflect the challenges of interpreting associated images or simply the accumulation of orthopedic hardware.

5 Discussion and Conclusion

As our results show, Pelphix is a potentially viable approach to robust SPR based on X-ray images. We showed that stochastic simulation of percutaneous fracture fixation, despite having no access to real image sequences, is a sufficiently realistic data source to enable sim-to-real transfer. While we expect adjustments to the simulation approach will close the gap even further, truly performative SPR algorithms for X-ray may rely on Pelphix-style simulation for pretraining, before fine-tuning on real image sequences to account for human-like behavior. Extending this approach to other procedures in orthopedic surgery, angiography, and interventional radiology will require task-specific simulation capable of modeling possibly more complex tool-tissue interactions and human-in-the-loop workflows. Nevertheless, Pelphix provides a viable first route toward X-ray-based surgical phase recognition, which we hope will motivate routine collection and interpretation of these data, in order to enable advances in surgical data science that ultimately improve the standard of care for patients.

Acknowledgements. This work was supported by NIH Grant No. R21EB028505 and Johns Hopkins University internal funds. Thank you to Demetries Boston, Henry Phalen, and Justin Ma for assistance with cadaver experiments.

References

1. Bier, B., et al.: X-ray-transform invariant anatomical landmark detection for pelvic trauma surgery. In: Frangi, A.F., Schnabel, J.A., Davatzikos, C., Alberola-López, C., Fichtinger, G. (eds.) MICCAI 2018. LNCS, vol. 11073, pp. 55–63. Springer, Cham (2018). https://doi.org/10.1007/978-3-030-00937-3_7
2. Caldwell, R., Kamionkowski, M.: Dark matter and dark energy. *Nature* **458**(7238), 587–589 (2009). <https://doi.org/10.1038/458587a>
3. Czempiel, T., Paschali, M., Ostler, D., Kim, S.T., Busam, B., Navab, N.: OperA: attention-regularized transformers for surgical phase recognition. In: de Bruijne, M., et al. (eds.) MICCAI 2021, Part IV. LNCS, vol. 12904, pp. 604–614. Springer, Cham (2021). https://doi.org/10.1007/978-3-030-87202-1_58
4. Da Col, T., Mariani, A., Deguet, A., Menciassi, A., Kazanzides, P., De Momi, E.: SCAN: system for camera autonomous navigation in robotic-assisted surgery. In: 2020 IEEE/RSJ International Conference on Intelligent Robots and Systems (IROS), pp. 2996–3002. IEEE (2021). <https://doi.org/10.1109/IROS45743.2020.9341548>
5. DiPietro, R., et al.: Segmenting and classifying activities in robot-assisted surgery with recurrent neural networks. *Int. J. Comput. Assist. Radiol. Surg.* **14**(11), 2005–2020 (2019). <https://doi.org/10.1007/s11548-019-01953-x>
6. Gao, C., et al.: SyntheX: scaling up learning-based X-ray image analysis through in silico experiments. *arXiv* (2022). <https://doi.org/10.48550/arXiv.2206.06127>
7. Guédon, A.C.P.: Deep learning for surgical phase recognition using endoscopic videos. *Surg. Endosc.* **35**(11), 6150–6157 (2020). <https://doi.org/10.1007/s00464-020-08110-5>

8. Hossain, M., Nishio, S., Hiranaka, T., Kobashi, S.: Real-time surgical tools recognition in total knee arthroplasty using deep neural networks. In: 2018 Joint 7th International Conference on Informatics, Electronics & Vision (ICIEV) and 2018 2nd International Conference on Imaging, Vision & Pattern Recognition (icIVPR), pp. 470–474. IEEE (2018). <https://doi.org/10.1109/ICIEV.2018.8641074>
9. Kadkhodamohammadi, A., et al.: Towards video-based surgical workflow understanding in open orthopaedic surgery. *Comput. Meth. Biomech. Biomed. Eng. Imaging Vis.* **9**(3), 286–293 (2021). <https://doi.org/10.1080/21681163.2020.1835552>
10. Kausch, L., et al.: C-Arm positioning for spinal standard projections in different intra-operative settings. In: de Bruijne, M., et al. (eds.) MICCAI 2021. LNCS, vol. 12904, pp. 352–362. Springer, Cham (2021). https://doi.org/10.1007/978-3-030-87202-1_34
11. Killeen, B.D., et al.: An autonomous X-ray image acquisition and interpretation system for assisting percutaneous pelvic fracture fixation. *Int. J. CARS* **18**, 1–8 (2023). <https://doi.org/10.1007/s11548-023-02941-y>
12. Killeen, B.D., et al.: Mixed reality interfaces for achieving desired views with robotic X-ray systems. *Comput. Meth. Biomech. Biomed. Eng. Imaging Vis.* **11**, 1–6 (2022). <https://doi.org/10.1080/21681163.2022.2154272>
13. Kim, K.P., et al.: Occupational radiation doses to operators performing fluoroscopically-guided procedures. *Health Phys.* **103**(1), 80 (2012). <https://doi.org/10.1097/HP.0b013e31824dae76>
14. Munawar, A., et al.: Virtual reality for synergistic surgical training and data generation. *Comput. Meth. Biomech. Biomed. Eng. Imaging Vis.* **10**, 1–9 (2021)
15. Padoy, N.: Machine and deep learning for workflow recognition during surgery. *Minim. Invasive Therapy Allied Technol.* **28**(2), 82–90 (2019). <https://doi.org/10.1080/13645706.2019.1584116>
16. Ronneberger, O., Fischer, P., Brox, T.: U-Net: convolutional networks for biomedical image segmentation. In: Navab, N., Hornegger, J., Wells, W.M., Frangi, A.F. (eds.) MICCAI 2015. LNCS, vol. 9351, pp. 234–241. Springer, Cham (2015). https://doi.org/10.1007/978-3-319-24574-4_28
17. Simonian, P.T., Routt Jr, M.L.C., Harrington, R.M., Tencer, A.F.: Internal fixation of the unstable anterior pelvic ring a biomechanical comparison of standard plating techniques and the retrograde medullary superior pubic ramus screw. *J. Orthop. Trauma* **8**(6), 476 (1994)
18. Unberath, M., et al.: DeepDRR – a catalyst for machine learning in fluoroscopy-guided procedures. In: Frangi, A.F., Schnabel, J.A., Davatzikos, C., Alberola-López, C., Fichtinger, G. (eds.) MICCAI 2018. LNCS, vol. 11073, pp. 98–106. Springer, Cham (2018). https://doi.org/10.1007/978-3-030-00937-3_12
19. Valderrama, N., et al.: Towards holistic surgical scene understanding. In: Wang, L., Dou, Q., Fletcher, P.T., Speidel, S., Li, S. (eds.) MICCAI 2022. Lecture Notes in Computer Science, vol. 13437, pp. 442–452. Springer, Cham (2022). https://doi.org/10.1007/978-3-031-16449-1_42
20. Varier, V.M., Rajamani, D.K., Goldfarb, N., Tavakkolmoghaddam, F., Munawar, A., Fischer, G.S.: Collaborative suturing: a reinforcement learning approach to automate hand-off task in suturing for surgical robots. In: 2020 29th IEEE International Conference on Robot and Human Interactive Communication (RO-MAN), pp. 1380–1386. IEEE (2020). <https://doi.org/10.1109/RO-MAN47096.2020.9223543>

21. Wu, J.Y., Tamhane, A., Kazanzides, P., Unberath, M.: Cross-modal self-supervised representation learning for gesture and skill recognition in robotic surgery. *Int. J. Comput. Assist. Radiol. Surg.* **16**(5), 779–787 (2021). <https://doi.org/10.1007/s11548-021-02343-y>
22. Zhang, B., et al.: Towards accurate surgical workflow recognition with convolutional networks and transformers. *Comput. Meth. Biomech. Biomed. Eng. Imaging Vis.* **10**(4), 349–356 (2022). <https://doi.org/10.1080/21681163.2021.2002191>
23. Zisimopoulos, O., et al.: DeepPhase: surgical phase recognition in CATARACTS videos. In: Frangi, A.F., Schnabel, J.A., Davatzikos, C., Alberola-López, C., Fichtinger, G. (eds.) *MICCAI 2018. LNCS*, vol. 11073, pp. 265–272. Springer, Cham (2018). https://doi.org/10.1007/978-3-030-00937-3_31